

# Fast thermal relaxation in cavity-coupled graphene bolometers with a Johnson noise read-out

Dmitri K. Efetov<sup>1\*</sup>, Ren-Jye Shiue<sup>2</sup>, Yuanda Gao<sup>3</sup>, Brian Skinner<sup>4</sup>, Evan D. Walsh<sup>2</sup>, Hyeonrak Choi<sup>2</sup>, Jiabao Zheng<sup>2</sup>, Cheng Tan<sup>3</sup>, Gabriele Grosso<sup>2</sup>, Cheng Peng<sup>2</sup>, James Hone<sup>3</sup>, Kin Chung Fong<sup>5</sup> and Dirk Englund<sup>1,2</sup>

**High sensitivity, fast response time and strong light absorption are the most important metrics for infrared sensing and imaging. The trade-off between these characteristics remains the primary challenge in bolometry. Graphene with its unique combination of a record small electronic heat capacity and a weak electron-phonon coupling has emerged as a sensitive bolometric medium that allows for high intrinsic bandwidths<sup>1–3</sup>. Moreover, the material's light absorption can be enhanced to near unity by integration into photonic structures. Here, we introduce an integrated hot-electron bolometer based on Johnson noise readout of electrons in ultra-clean hexagonal-boron-nitride-encapsulated graphene, which is critically coupled to incident radiation through a photonic nanocavity with  $Q = 900$ . The device operates at telecom wavelengths and shows an enhanced bolometric response at charge neutrality. At 5 K, we obtain a noise equivalent power of about  $10 \text{ pW Hz}^{-1/2}$ , a record fast thermal relaxation time,  $< 35 \text{ ps}$ , and an improved light absorption. However the device can operate even above 300 K with reduced sensitivity. We work out the performance mechanisms and limits of the graphene bolometer and give important insights towards the potential development of practical applications.**

Since the invention of the bolometer, its main design principles have relied on efficient light absorption into a low-heat-capacity material and its exceptional thermal isolation from the environment. Though reduced thermal coupling to its surroundings allows for an enhanced thermal response, it in turn strongly increases the thermal time constant and dramatically lowers the detector's bandwidth. Due to its record-low electronic heat capacity  $C_e$  (refs<sup>1,4,5</sup>) and weak heat dissipation<sup>5,6</sup>, absorbed radiation can give rise to an electron temperature,  $T_e$ , that can be dramatically higher than the lattice temperature,  $T_s$ , while maintaining a fast thermal relaxation time (Fig. 1a). These unique thermal properties and its broad-band photon absorption from the UV to GHz frequencies<sup>7</sup> make graphene a promising platform for ultrasensitive and ultrafast hot electron bolometers, calorimeters and single-photon detectors for low-energy photons<sup>2,8,9</sup>.

Previous studies have demonstrated graphene's potential as a sensitive bolometer<sup>3,10,11</sup>; however, many challenges remain for real applications. Most experiments utilized graphene on a  $\text{SiO}_2$  substrate with a slow d.c. transport readout. To achieve a high response, graphene's weak temperature-dependent resistance  $\Delta R(T_e)/\Delta T_e$  had to be artificially increased by introducing disorder<sup>12</sup>, patterning

nanostructures<sup>13</sup> or opening a bandgap in bilayer graphene<sup>3</sup>. As disorder introduces charge fluctuations at the charge neutrality point (CNP), it limits the detector's response, as the lowest  $C_e$  values in close vicinity to the CNP cannot be reached. Low light absorption of only  $\sim 2.3\%$  (below THz wavelengths)<sup>7,14,15</sup> makes these devices more impractical.

It was recently shown that it is possible to use a universal  $T_e$  readout utilizing microwave frequency Johnson noise (JN), which is emitted by thermally agitated electrons in graphene<sup>1,2,5,9,16</sup>. This direct  $T_e$  readout scheme does not require a large  $\Delta R(T_e)/\Delta T_e$  and allows use of ultraclean hexagonal boron nitride (hBN) encapsulated graphene devices without sacrificing the detector's sensitivity. In state-of-the-art devices the carrier density can be tuned to ultrasmall values of  $n < 10^{10} \text{ e cm}^{-2}$  (ref.<sup>17</sup>) where  $C_e$  can reach record low values of just one Boltzmann constant  $k_B$ . Moreover, recent progress in the critical coupling of graphene to resonant photonic cavities<sup>18,19</sup> and to antennas<sup>2,13</sup> showed that one can achieve close to unity light absorption into graphene for a broad range of frequencies.

In this manuscript we combine all of the above techniques in a proof-of-concept device. Figure 1b shows the schematics and the operation principle of the bolometer. A high-quality hBN-G-hBN graphene heterostructure is integrated onto a suspended silicon photonic crystal cavity (PCC), with a linear three-hole (L3) defect, which serves to form confined optical cavity modes. The resonant cavity mode of the PCC (Fig. 1c) is critically coupled to the telecom spectrum and evanescently overlaps with the graphene sheet<sup>18</sup>. To maximize heat generation and to minimize heat dissipation, the graphene stack is etched into a circle with  $5 \mu\text{m}$  diameter, which corresponds to the expected length scale over which the electron temperature relaxes back to thermal equilibrium<sup>20</sup>. It is further connected to gold leads with narrow, resistive graphene channels. To effectively transmit the microwave Johnson noise signal through the circuit, the high resistance of the graphene ( $R \sim 20 \text{ k}\Omega$ ) is impedance matched to the microwave transmission line ( $50 \Omega$ ) by the addition of a carefully chosen inductor and capacitor. The so formed resonant RLC circuit has a resonance frequency of  $\sim 70 \text{ MHz}$  with a bandwidth of  $\sim 6 \text{ MHz}$ , and allows transmission of most of the JN power (JNP) (see Supplementary Information) to a low-noise amplifier (LNA) and a heterodyne circuit, which are situated at room temperature. The radio frequency circuit forms the JN readout scheme, and its voltage output is directly proportional to the emitted JNP.

<sup>1</sup>ICFO - Institut de Ciències Fòniques, The Barcelona Institute of Science and Technology, Barcelona, Spain. <sup>2</sup>Department of Electrical Engineering and Computer Science, Massachusetts Institute of Technology, Cambridge, MA, USA. <sup>3</sup>Department of Mechanical Engineering, Columbia University, New York, NY, USA. <sup>4</sup>Department of Physics, Massachusetts Institute of Technology, Cambridge, MA, USA. <sup>5</sup>Raytheon BBN Technologies, Quantum Information Processing Group, Cambridge, MA, USA. \*e-mail: [dmitri.efetov@icfo.eu](mailto:dmitri.efetov@icfo.eu)

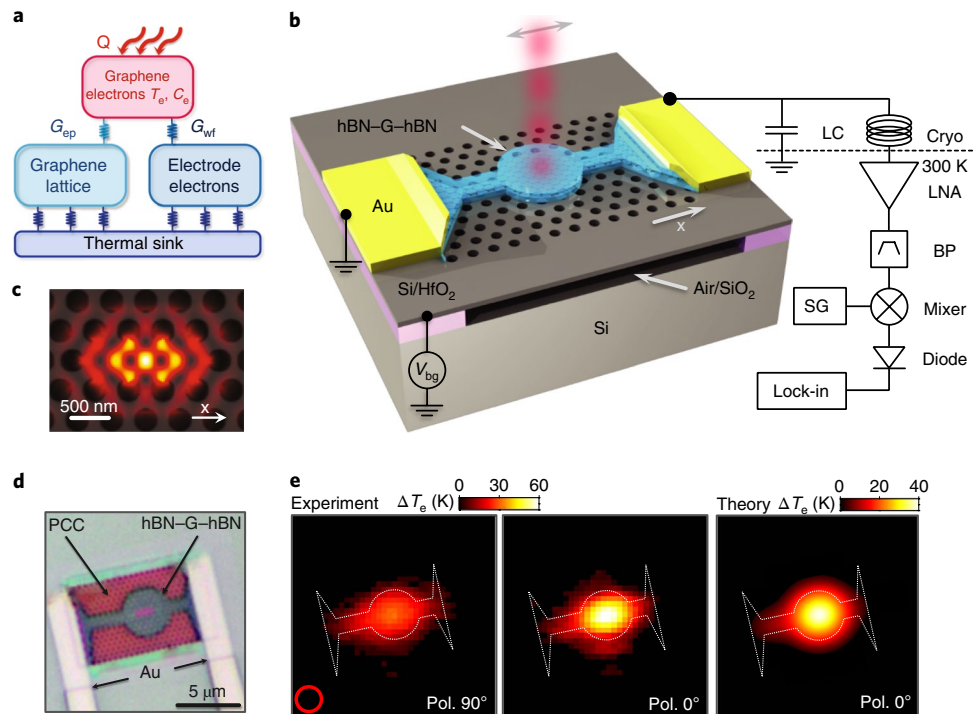


**Fig. 1 | Device schematics and operation principle.** **a**, Schematics of heat dissipation channels of irradiated hot electrons in graphene. Primary mechanism includes the WF law ( $G_{WF}$ ) and e-ph scattering ( $G_{ep}$ ). **b**, Schematic of the device, which consists of a side-contacted hBN-G-hBN heterostructure on top of a suspended silicon L3 PCC. The device is impedance matched to a LC network at cryogenic temperatures and is read out by a heterodyne JN thermometry scheme at room temperature, which allows for an accurate reading of  $T_e$ . BP, bandpass filter; SG, signal generator. **c**, Resonant modes form in the L3 PCC as is seen in the calculated spatial electric field intensity  $|E|^2$  profile. **d**, Optical microscope image of the device. **e**, Map of the bolometric response of the device as a function of laser spot position (red circle, laser spot size) measured at  $T_s = 5$  K and  $\Delta V_{bg} = 0$  V. Left,  $\Delta T_e$  for  $90^\circ$  polarized light (PCC off resonance); middle, for  $0^\circ$  polarized light (PCC on resonance); and right, theoretical model for  $0^\circ$  polarized light. Overall the bolometric response occurs only when the laser beam is injected onto the graphene covered area, and is strongly enhanced when the PCC mode is on resonance.

By applying a gate voltage  $\Delta V_{bg}$  (referenced to the CNP) to the PCC one can control the carrier density of the graphene sheet.

The device is probed at  $T_s = 5$  K and  $\Delta V_{bg} = 0$  V with linearly polarized excitation pulses from a tunable near-infrared laser, which are normally incident onto the device through a cross-polarized confocal scanning set-up<sup>21</sup> (Supplementary Information). Simultaneously to spatial scanning of the laser, the calibrated JNP is read out<sup>1</sup>. As the JNP is directly proportional to  $T_e$  (Supplementary Information), we are able to obtain the electronic temperature increase due to laser excitation  $\Delta T_e$  for each laser spot position. Figure 1d shows the optical image of the device and Fig. 1e the  $\Delta T_e$  spatial map for  $0^\circ$  and  $90^\circ$  polarized light at the PCCs resonant frequency of 1,532 nm and an incident power of  $P_{in} = 5.4 \mu\text{W}$ . Here, a sizeable  $\Delta T_e$  increase is generated only when the laser is incident directly onto the graphene, confirming that the JN readout is only sensitive to thermal noise inside the graphene channel. As the PCC's resonant mode only couples to light with polarization along the  $x$ -axis, one can compare the response off ( $90^\circ$  polarization) and on ( $0^\circ$  polarization) resonance (Fig. 1e, left and middle). When off resonance,  $\Delta T_e$  is roughly constant over the entire graphene region, assuming that 2.3% of the incident light is homogeneously absorbed in the whole graphene region. Whereas when on resonance, in addition to direct light absorption, light is also resonantly coupled into the PCC. The resonant mode interacts with graphene and gives a strong rise to an enhancement of  $\Delta T_e$  in the cavity region. With the thermal model presented in Fig. 1a (Supplementary Information), the theoretically expected  $\Delta T_e$  map is calculated (Fig. 1e right), and shows very good agreement with experimental findings.

To characterize the enhancement of light absorption by the PCC we perform measurements of the reflection spectrum of the irradiated cavity before the deposition of the hBN-G-hBN stack and after. Figure 2a shows the fundamental mode of the pure cavity with a resonance mode at 1,512.8 nm and a quality factor of  $Q \sim 7,000$ . After the hBN-G-hBN deposition, the cavity resonance is red-shifted to 1,531.7 nm and its  $Q$  drops to  $\sim 900$ . Here the shift of the mode is mainly due to hBN's high dielectric constant of  $\sim 3.9$ , while its broadening is caused by the light absorption in graphene. From coupled mode theory<sup>18</sup>, we estimate that the total absorption of the cavity resonant field into graphene is  $\sim 45\%$ .

Overall the enhanced light absorption strongly amplifies the photoresponse. Figure 2b shows  $\Delta T_e$  as a function of incident laser wavelength for  $0^\circ$  (on) and  $90^\circ$  (off) polarized light with respect to the cavity  $x$ -axis (Fig. 1c). In the on state at a resonance wavelength of 1,531.7 nm,  $\Delta T_e$  is enhanced by a factor of  $\sim 3$  and follows a sinusoidal dependence as a function of the polarization angle (Fig. 2b inset). From the difference of the  $\Delta T_e$  increase on and off resonance, we can deduce that the total absorption in graphene is enhanced from 2.3% to more than 7%. Since graphene absorbs  $\sim 45\%$  of the cavity field, we extract a coupling efficiency of the cavity field to normal incidence laser light to be  $\sim 10\%$ , consistent with simulation results. With improved fabrication, however, one can expect near-unity absorption through critical coupling to a waveguide<sup>22,23</sup> or free-space<sup>24,25</sup>, and experimentally  $>90\%$  absorption from a photonic nanocavity into graphene has already been demonstrated<sup>18</sup>.

We now probe  $\Delta T_e$  as a function of absorbed laser power  $P$  (assuming 7% incident light absorption) at  $T_s = 5$  K and a measurement time of  $t_{in} = 1$  s (Fig. 3a). Here the  $\Delta T_e(P)$  dependence

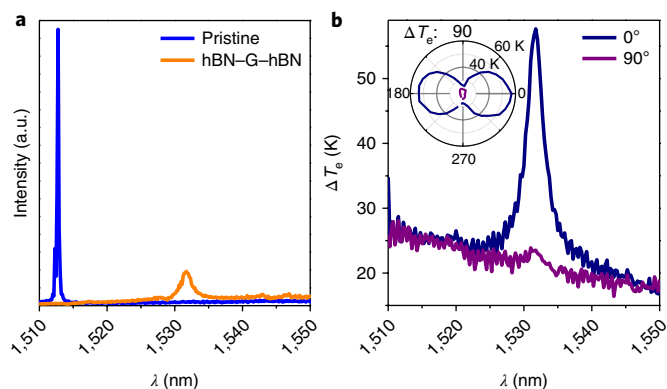


**Fig. 2 | Role of the PCC in enhancement of the bolometric response.** **a**, Reflection spectra of the normally excited PCC cavity mode before and after the deposition of the hBN-G-hBN stack. Due to light absorption in the graphene and hBNs high dielectric constant the resonance is broadened and red-shifted. **b**, Bolometric response as a function of the incident wavelength for 0° (on) and 90° (off) linearly polarized light, at  $T_s = 5$  K and  $\Delta V_{bg} = 0$  V. Inset shows sinusoidal polarization angle dependence of  $\Delta T_e$  for different wavelengths on (blue, 1,532.5 nm) and off (purple, 1,520 nm) resonance.

transitions from a linear to a sublinear dependence with increased  $P$ , and is overall strongly reduced at elevated temperatures (inset Fig. 3a). We can model this behaviour with the two-dimensional heat transfer equation below (equation (1)), which takes into account the two main mechanisms: electronic dissipation through the Wiedemann–Franz (WF) law (first term) and through electron–phonon (e–ph) interactions (second term):

$$\vec{q} = -\vec{\nabla} \cdot [\kappa \vec{\nabla} T_e] + \Sigma_{ep} [T_e^3 - T_s^3], \quad (1)$$

where  $\Sigma_{ep}$  is the e–ph coupling strength,  $\kappa = (\pi^2 k_B T_e) / 3e\rho$  the thermal conductivity and  $\rho$  the device resistivity, which is extracted from transport measurements (Supplementary Information). Numerical modelling with only one fitting parameter  $\Sigma_{ep} = 0.038 \text{ W m}^{-2} \text{ K}^{-3}$  produces a good match with the experiment and agrees well with previously reported values<sup>5</sup>. We can qualitatively understand the

sub-linear behaviour by the overall enhancement of the electronic thermal conductivity  $G_{th}$  at higher  $T_s$ , where both WF and e–ph dissipation channels are strongly enhanced. The bolometric response due to laser heating is furthermore consistent with the response through Joule heating of the sample with a large current<sup>1</sup> (Fig. 3a). Here minor deviations can be attributed to saturable light absorption in graphene at higher laser powers<sup>26</sup>.

Ultimately, the bolometric response is limited by the electronic thermal conductivity,  $G_{th}$ , through the simple relation  $\Delta T_e = P/G_{th}$ , which is a direct consequence of equation (1). From measurements at various  $T_s$  with a fixed  $P = 100$  nW, we obtain the  $G_{th}(T_s)$  dependence (Fig. 3b). It is in good agreement with the heat dissipation model, and follows a linear WF dependence at low  $T_s$  and a power law e–ph dependence at higher  $T_s$ . Since both  $C_e$  and  $G_{th}$  are expected to be strongly reduced at the CNP<sup>5</sup>, we test  $\Delta T_e$  as a function of gate voltage  $\Delta V_{bg}$ . Figure 3c plots  $\Delta T_e(\Delta V_{bg})$  for  $P = 10$  nW and compares it to  $R(\Delta V_{bg})$  (both taken at  $T_s = 5$  K). The response sharply increases by a factor  $\sim 3$  at the CNP and qualitatively follows the same dependence as  $R(\Delta V_{bg})$ . However, the enhancement of the response at the CNP is predicted to be several orders of magnitude higher at mK temperatures, as thermal broadening of the Fermi energy is reduced and  $C_e$  is dramatically lowered<sup>1,2</sup>.

In analogy to previous work on graphene pn-junctions<sup>27–29</sup>, we can now test the thermal relaxation time of the hot electrons,  $\tau$ , which defines the intrinsic bandwidth limit of the detector.  $\tau$  can be probed by the excitation of the bolometer with two  $t_d$  time-delayed pulses (Supplementary Information), where the first pulse heats the electrons to an elevated  $T_e$ , and the second pulse heats the electron gas further. For  $t_d \sim 0$  ps, the  $T_e$  rise due to the second pulse is smaller than the  $T_e$  rise for the first pulse, because of the non-linear  $\Delta T_e(P)$  dependence in Fig. 3a. This results in a greatly diminished integrated JNP signal around  $t_d \sim 0$  ps. Figure 4a shows the normalized JNP as a function of  $t_d$ ,  $\text{JNP}(t_d)/\text{JNP}(120 \text{ ps})$ .

The curves follow an inverse exponential form where the half-width at half-maximum (HWHM) of the central dip defines  $\tau$ , which is in very good agreement with previous studies<sup>3,27–31</sup>. As  $G_{th}$  at low  $T_e$  is dominated by WF,  $\tau$  is on the order of only  $\sim 30$  ps, which is much faster than one would expect in e–ph limited device architectures<sup>9</sup>.

From the above device characterization, we can define the bolometer's performance characteristics, the noise equivalent power (NEP) and the intrinsic reset time, which is defined by  $\tau$

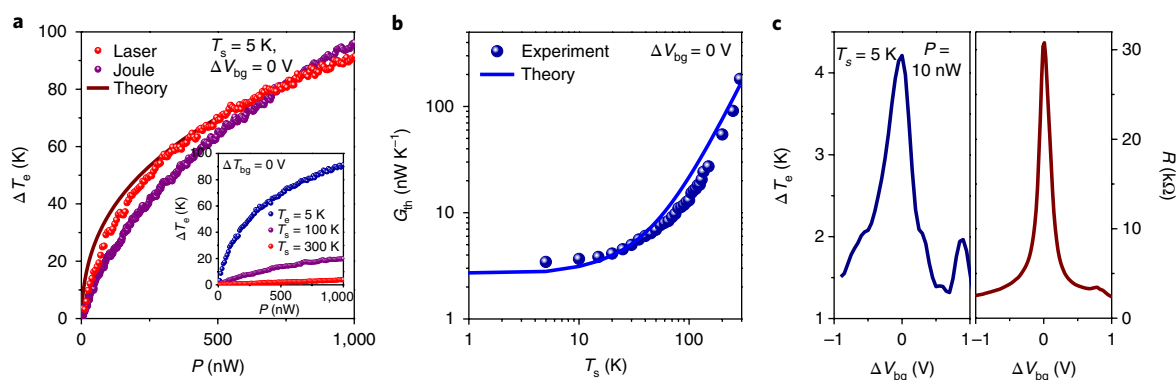


**Fig. 3 | Bolometric response.** **a**, Bolometric response  $\Delta T_e$  as a function of absorbed heating power  $P$ , for laser and Joule heating at  $\Delta V_{bg} = 0$  V and  $T_s = 5$  K. Inset shows  $\Delta T_e$  for laser heating at various device temperatures  $T_s$ . **b**, The extracted thermal conductance  $G_{th} = P/\Delta T_e$  as a function of  $T_s$ . Overall the experimental results in **a** and **b** are consistent with a heat dissipation model based on the WF law and e–ph coupling (theory fits using equation (1)). As the bolometric response is mainly limited by thermally activated dissipation mechanisms, it is strongly reduced at elevated  $T_s$ . **c**, Gate dependence of  $\Delta T_e(\Delta V_{bg})$  for  $P = 10$  nW (left) and  $R(\Delta V_{bg})$  (right), both measured at  $T_s = 5$  K. The curves show qualitatively similar dependence with a strong enhancement of  $\Delta T_e$  at the CNP, due to a reduced  $C_e$ .

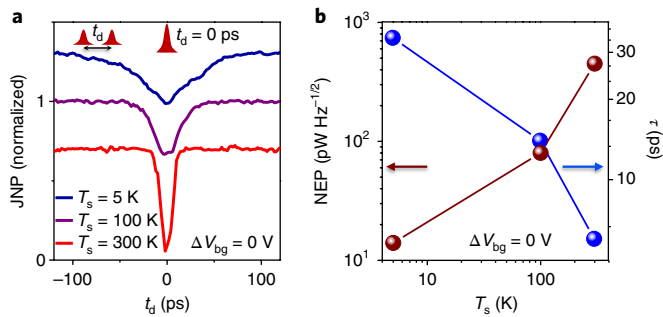


**Fig. 4 | Detector performance.** **a**, Normalized  $JNP(t_d)/JNP(120\text{ ps})$  probed with two  $t_d$  time-delayed laser pulses at various device temperatures  $T_s$  and at  $V_{bg} = 0\text{ V}$  (graphs are offset for clarity). From the HWHM of the dip around at  $t_d = 0\text{ ps}$  we extract the intrinsic thermal relaxation time of the bolometer  $\tau$ . As  $G_{th}$  becomes reduced at low  $T_s$ ,  $\tau$  in turn increases. **b**, NEP and  $\tau$  as a function of  $T_s$  at  $\Delta V_{bg} = 0\text{ V}$ . We extract a NEP  $\sim 10\text{ pW Hz}^{-1/2}$  and an intrinsic reset time of  $\tau \sim 30\text{ ps}$  at  $T_s = 5\text{ K}$ , the bolometer has a unique combination of high readout sensitivity and high intrinsic bandwidth. It has no hard limit on the operation temperature.

(Fig. 4b). Here the calibration of the bolometric readout scheme gives an overall sensitivity of  $\delta T_c \sim 10\text{ mK}$  for a measurement time of  $t_{in} = 1\text{ s}$  (Supplementary Information), which together with the  $G_{th}$  values from Fig. 3b allows extraction of the NEP values of the bolometer. The bolometer has no hard limit on the operation temperature and can be operated above liquid nitrogen and even room temperatures, with typical values reaching a NEP  $\sim 10\text{ pW Hz}^{-1/2}$  and a  $\tau \sim 30\text{ ps}$  at  $T_s = 5\text{ K}$  and  $\Delta V_{bg} = 0\text{ V}$ . At the CNP, the NEP is strongly reduced, while  $\tau$  only weakly varies with  $\Delta V_{bg}$  (refs.<sup>28,32</sup>). Generally, while the NEP is dramatically reduced at low  $T_s$ ,  $\tau$  is increased.

As is given by the Dicke radiometer relation<sup>33</sup>, the temperature sensitivity of the system is given by  $\delta T = (T + T_{sys}) / (B t_{in})^{1/2}$ , where  $B$  is the measurement bandwidth,  $t_{in}$  the measurement time and  $T_{sys}$  the system noise, which is dominated by the LNA (Supplementary Information). From this relation it is clear that the sensitivity can be dramatically reduced by cooling the entire measurement circuit, the use of quantum-limited amplifiers and by increasing  $B$ , and it was shown theoretically that the presented device concept could reach an NEP  $\sim 10^{-20}\text{ W Hz}^{-1/2}$  at  $T_s = 10\text{ mK}$  (ref.<sup>2</sup>). Given the ultrafast intrinsic bandwidth of the bolometer, its ultimate detection speed is mainly limited by the readout electronics. While state-of-the-art LNAs can operate at frequencies above 10 GHz, such a fast readout would dramatically lower  $\Delta T_c$  (as follows from the Dicke relationship (Supplementary Information)). In this regard, a practical graphene bolometer design would have to operate at a carefully chosen trade-off space between the desired measurement sensitivity and a fast readout, which is captured by the value of the NEP. In addition, while the integration of the bolometer into resonant light structures will enhance light absorption, it will sacrifice graphene's broadband absorption properties. It is, however, feasible that one could develop small bolometer arrays, similar to the recently developed microwave single-photon detector arrays, where each bolometer is individually coupled to a PCC with a different resonant frequency, making the array sensitive to a broad range of frequencies.

In conclusion, the presented study shows the promises and challenges towards practical applications of graphene-based bolometers. With its improved light absorption, high sensitivity, ultrafast thermal relaxation time, no limitations on its operation temperature and the potential for mid-infrared and THz applications, this proof-of-concept device provides unique characteristics for the development of advanced bolometers with new functionalities.

## Methods

Methods, including statements of data availability and any associated accession codes and references, are available at <https://doi.org/10.1038/s41565-018-0169-0>.

Received: 28 November 2017; Accepted: 15 May 2018;

Published online: 11 June 2018

## References

- Fong, K. C. & Schwab, K. C. Ultrasensitive and wide-bandwidth thermal measurements of graphene at low temperatures. *Phys. Rev. X* **2**, 031006 (2012).
- McKitterick, C. B., Prober, D. E. & Karasik, B. S. Performance of graphene thermal photon detectors. *J. Appl. Phys.* **113**, 044512 (2013).
- Yan, J. et al. Dual-gated bilayer graphene hot-electron bolometer. *Nat. Nanotech.* **7**, 472–478 (2012).
- Balandin, A. A. Thermal properties of graphene and nanostructured carbon materials. *Nat. Mater.* **10**, 569–581 (2011).
- Fong, K. C. et al. Measurement of the electronic thermal conductance channels and heat capacity of graphene at low temperature. *Phys. Rev. X* **3**, 041008 (2013).
- Crossno, J. et al. Observation of the Dirac fluid and the breakdown of the Wiedemann–Franz law in graphene. *Science* **351**, 1058–1061 (2016).
- Mak, K. F. et al. Measurement of the optical conductivity of graphene. *Phys. Rev. Lett.* **101**, 196405 (2008).
- Walsh, E. D. et al. Graphene-based Josephson-junction single-photon detector. *Phys. Rev. Appl.* **8**, 024022 (2017).
- Du, X., Prober, D. E., Vora, H. & McKitterick, C. B. Graphene-based bolometers. *Graphene 2D Mater.* **1**, 1–22 (2014).
- Vora, H., Kumaravadivel, P., Nielsen, B. & Du, X. Bolometric response in graphene based superconducting tunnel junctions. *Appl. Phys. Lett.* **100**, 153507 (2012).
- Cai, X. et al. Sensitive room-temperature terahertz detection via the photothermoelectric effect in graphene. *Nat. Nanotech.* **9**, 814–819 (2014).
- Han, Q. et al. Highly sensitive hot electron bolometer based on disordered graphene. *Sci. Rep.* **3**, 3533 (2013).
- El Fatimy, A. et al. Epitaxial graphene quantum dots for high-performance terahertz bolometers. *Nat. Nanotech.* **11**, 335–338 (2016).
- Nair, R. R. et al. Fine structure constant defines visual transparency of graphene. *Science* **320**, 1308 (2008).
- Li, Z. Q. et al. Dirac charge dynamics in graphene by infrared spectroscopy. *Nat. Phys.* **4**, 532–535 (2008).
- McKitterick, C. B., Prober, D. E. & Rooks, M. J. Electron-phonon cooling in large monolayer graphene devices. *Phys. Rev. B Condens. Matter* **93**, 075410 (2016).
- Dean, C. R. et al. Boron nitride substrates for high-quality graphene electronics. *Nat. Nanotech.* **5**, 722–726 (2010).
- Gan, X. et al. Strong enhancement of light–matter interaction in graphene coupled to a photonic crystal nanocavity. *Nano Lett.* **12**, 5626–5631 (2012).
- Bao, Q. & Loh, K. P. Graphene photonics, plasmonics, and broadband optoelectronic devices. *ACS Nano* **6**, 3677–3694 (2012).
- Gabor, N. M. et al. Hot carrier–assisted intrinsic photoresponse in graphene. *Science* **334**, 648–652 (2011).
- Gao, Y. et al. High-speed electro-optic modulator integrated with graphene–boron nitride heterostructure and photonic crystal nanocavity. *Nano Lett.* **15**, 2001–2005 (2015).
- Shiue, R.-J. et al. Enhanced photodetection in graphene-integrated photonic crystal cavity. *Appl. Phys. Lett.* **103**, 241109 (2013).
- Takano, H., Song, B. S., Asano, T. & Noda, S. Highly efficient multi-channel drop filter in a two-dimensional hetero photonic crystal. *Opt. Express* **14**, 3491–3496 (2006).
- Zheng, J., Barton, R. A. & Englund, D. Broadband coherent absorption in chirped-planar-dielectric cavities for 2D-material-based photovoltaics and photodetectors. *ACS Photonics* **1**, 768–774 (2014).
- Piper, J. R. & Fan, S. Total absorption in a graphene monolayer in the optical regime by critical coupling with a photonic crystal guided resonance. *ACS Photonics* **1**, 347–353 (2014).
- Marini, A., Cox, J. D. & de Abajo, F. J. G. Theory of graphene saturable absorption. *Phys. Rev. B* **95**, 125408 (2017).
- Tielrooij, K. J. et al. Generation of photovoltage in graphene on a femtosecond timescale through efficient carrier heating. *Nat. Nanotech.* **10**, 437–443 (2015).
- Graham, M. W., Shi, S.-F., Ralph, D. C., Park, J. & McEuen, P. L. Photocurrent measurements of supercollision cooling in graphene. *Nat. Phys.* **9**, 103–108 (2012).
- Shiue, R.-J. et al. High-responsivity graphene–boron nitride photodetector and autocorrelator in a silicon photonic integrated circuit. *Nano Lett.* **15**, 7288–7293 (2015).

30. Tielrooij, K. J. et al. Out-of-plane heat transfer in van der Waals stacks: electron–hyperbolic phonon coupling. *Nat. Nanotech.* **13**, 41–46 (2018).
31. Sun, D. et al. Ultrafast hot-carrier-dominated photocurrent in graphene. *Nat. Nanotech.* **7**, 114–118 (2012).
32. Tielrooij, K.-J. et al. Out-of-plane heat transfer in van der Waals stacks through electron–hyperbolic phonon coupling. *Nat. Nanotech.* **13**, 41–46 (2018).
33. Dicke, R. H. The measurement of thermal radiation at microwave frequencies. *Rev. Sci. Instrum.* **17**, 268–275 (1946).

### Acknowledgements

We thank L. Levitov, D. Prober, P. Kim and F. Koppens for fruitful discussions. D.K.E. acknowledges support from the Ministry of Economy and Competitiveness of Spain through the Severo Ochoa programme for Centres of Excellence in R&D (SEV-2015-0522), Fundació Privada Cellex, Fundació Privada Mir-Puig, the Generalitat de Catalunya through the CERCA program and the La Caixa Foundation. D.E. acknowledges support from the Office of Naval Research under grant no. N00014-14-1-0349. Y.G., C.T. and J.H. acknowledge support from the US Office of Naval Research, grant N00014-13-1-0662. K.C.F. acknowledges support from Raytheon BBN Technologies. B.S. was supported as part of the MIT Center for Excitonics, an Energy Frontier Research Center funded by the US Department of Energy, Office of Science, Basic Energy Sciences under award no. DE-SC0001088. J.Z. carried out research in part at the Center for Functional Nanomaterials, Brookhaven National Laboratory, which

is supported by the US Department of Energy, Office of Basic Energy Sciences, under contract no. DE-SC0012704. This work is supported in part by the Semiconductor Research Corporation's NRI Center for Institute for Nanoelectronics Discovery and Exploration (INDEX).

### Author contributions

D.K.E., K.C.F. and D.E. conceived and designed the experiments. D.K.E. and R.-J.S. performed the experiments. D.K.E. analysed the data. B.S. performed the theoretical modelling of the data. Y.G., C.T., C.P., H.C., E.D.W., J.Z. and G.G. contributed materials/analysis tools. J.H., K.C.F. and D.E. supported the experiments. D.K.E. wrote the paper.

### Competing interests

The authors declare no competing interests.

### Additional information

**Supplementary information** is available for this paper at <https://doi.org/10.1038/s41565-018-0169-0>.

**Reprints and permissions information** is available at [www.nature.com/reprints](http://www.nature.com/reprints).

**Correspondence and requests for materials** should be addressed to D.K.E.

**Publisher's note:** Springer Nature remains neutral with regard to jurisdictional claims in published maps and institutional affiliations.

## Methods

**Device fabrication.** The hBN-graphene-hBN stacks were exfoliated and assembled using a van der Waals assembly technique and then transferred onto the PCC cavity. The total thickness of the two hBN layers is around 30 nm. We patterned the hBN-graphene-hBN stack with hydrogen-silsesquioxane (HSQ) resist and  $\text{CHF}_3 + \text{O}_2$  plasma exposed the edges of graphene, which was subsequently contacted by Cr/Pd/Au (1/20/50 nm) metal leads using electron-beam evaporation. The L3 PCC cavities were fabricated on a silicon-on-insulator wafer using a series of electron-beam lithography, reactive ion etching and a wet-etch undercut of the insulator to produce free-standing membranes. The top silicon membrane has a thickness of  $\sim 220$  nm with a PCC lattice period of  $a = 440$  nm and

an air hole radius  $r = 0.29a$ . A linear three-hole (L3) defect in the middle of the PCC lattice serves to form confined optical cavity modes.

**Optical measurements.** The devices were illuminated with a scanning cross-polarized confocal microscope set-up. The reflection from the cavity was collected and coupled to a spectrometer to analyse its spectrum. For time-resolved measurements we used laser pulses from an optical parametric oscillator (OPO) pump by a Ti:Sapphire mode-lock laser (Mira-HP, Coherent). The pulse duration is 250 fs with a repetition rate of 78 MHz.

**Data availability.** The data that support the findings of this study are available from the corresponding author upon reasonable request.